Nanoporous BiVO₄ Photoanodes with Dual-Layer Oxygen Evolution Catalysts for Solar Water Splitting

Tae Woo Kim **and** Kyoung-Shin Choi*

Department of Chemistry, University of Wisconsin-Madison, Madison, WI 53706, USA.

*Corresponding author. E-mail: kschoi@chem.wisc.edu

Bismuth vanadate (BiVO₄) has a band structure well-suited for potential use as a photoanode in solar water splitting, but it suffers from poor electron-hole separation. Here we demonstrate that a nanoporous morphology (specific surface area of 31.8 m²/g) effectively suppresses bulk carrier recombination without additional doping, manifesting an electron-hole separation yield of 0.90 at 1.23 V vs. the reversible hydrogen electrode (RHE). We enhanced the propensity for surface-reaching holes to instigate water splitting chemistry by serially applying two different oxygen evolution catalyst (OEC) layers, FeOOH and NiOOH, which reduces interface recombination at the BiVO₄/OEC junction while creating a more favorable Helmholtz layer potential drop at the OEC/electrolyte junction. The resulting BiVO₄/FeOOH/NiOOH photoanode achieves a photocurrent density of 2.73 mA/cm² at a potential as low as 0.6 V vs. RHE.

N-type BiVO₄ has recently emerged as a promising photoanode for use in water splitting photoelectrochemical cells because it absorbs a substantial portion of the visible spectrum (bandgap energy, *ca.* 2.4 eV) and has a favorable conduction band (CB) edge position very near the thermodynamic H₂ evolution potential (*1, 2*). However, the solar to hydrogen (STH) conversion efficiency achieved by BiVO₄ to date has been far below what is expected because the material suffers from poor electron-hole separation yield (ϕ_sep) (*2–6*). Previous efforts to improve ϕ_sep of BiVO₄ mainly focused on doping studies, which were intended to improve its poor electron transport properties (*2, 6–12*).

Here we demonstrate that a high surface area nanoporous BiVO₄ electrode composed of particles smaller than its hole diffusion length can effectively increase ϕ_sep without additional doping. Furthermore, we investigated the effect of an oxygen evolution catalyst (OEC) layer on the interfacial recombination at the BiVO₄/OEC junction, water oxidation kinetics, and the Helmholtz layer potential drop at the OEC/electrolyte junction using two different OECs, FeOOH and NiOOH. Our understanding of the BiVO₄/OEC/electrolyte junction resulted in the development of a new strategy to serially apply dual layers of OECs that can optimize both the BiVO₄/OEC and the OEC/electrolyte junctions simultaneously, enabling efficient utilization of surface reaching holes for solar water oxidation.

Nanoporous BiVO₄ electrodes were prepared by first electrochemically depositing BiOI electrodes and then applying a dimethylsulfoxide (DMSO) solution of vanadyl acetylacetonate [VO(acac)₂] onto their surface and heating in air at 450°C for 2 hours (See Supplementary Materials for experimental details). A schematic overview of the synthesis procedure is shown in fig. S1. The specific advantage of using BiOI is that its two-dimensional (2D) crystal structure enables electrodeposition of extremely thin plates (*ca.* 20 nm) with sufficient voids between them (Fig. 1A). These voids inhibit grain growth of BiVO₄ during the conversion process, resulting in nanoporous BiVO₄ electrodes.

In a previous attempt to prepare nanoporous BiVO₄ (*13*), we used an NH₄OH solution of V₂O₅ as the vanadium source, which could not easily wet the BiOI surface because air in the voids between the BiOI plates

renders the surface highly hydrophobic (fig. S2). Thus, the distribution of V₂O₅ was uneven, few BiVO₄ nucleation processes were induced within a single 2D BiOI sheet, and the resulting electrodes manifested limited porosity (Fig. 1, B and C). The use of comparatively hydrophobic VO(acac)₂/DMSO solution overcame this problem and resulted in a remarkable increase in surface area. The top-view and side-view SEM images show the formation of much smaller BiVO₄ nanoparticles (mean particle size = 76 ± 5 nm, fig. S3) creating a three-dimensional nanoporous network (Fig. 1, D to F).

N₂ adsorption-desorption-isotherm measurements show that the nanoporous BiVO₄ electrode contains micropores within BiVO₄ particles as well as mesopores and macropores between BiVO₄ nanoparticles (fig. S4 and table S1) (*14*). The specific surface area of the nanoporous BiVO₄ electrode was estimated to be 31.8 ± 2.3 m²/g based on a fitting analysis using the Brunauer-Emmett-Teller (BET) equation (*14*). BiVO₄ electrodes prepared using other synthesis methods (e.g., metal organic decomposition, spray deposition, direct electrodeposition of BiVO₄) possess limited surface areas, and no attempts to measure surface areas of these samples were reported (*2*).

The purity and crystal structure of the nanoporous BiVO₄ electrode (monoclinic scheelite structure) were confirmed by X-ray diffraction (fig. S5). The bandgap of the nanoporous BiVO₄ electrode was estimated to be *ca.* 2.50 to 2.55 eV using UV-vis absorption spectra (fig. S6), which is slightly larger than the bandgap of BiVO₄ samples prepared by other methods that result in larger grain composition (*ca.* 2.4 eV) (*13, 15*).

The photoelectrochemical properties were first examined in the presence of 1 M sodium sulfite (Na₂SO₃), which served as the hole scavenger. The oxidation of sulfite is thermodynamically and kinetically more facile than oxidation of water (*11, 13, 15–18*), and, therefore, measuring photocurrent for sulfite oxidation enables investigation of the photoelectrochemical properties of BiVO₄ independently of its poor water oxidation kinetics. A typical photocurrent-potential (*J-V*) curve of the sulfite oxidation with nanoporous BiVO₄ is shown in Fig. 2A. A very early photocurrent onset potential, 0.1 V vs. RHE, and a rapid increase in photocurrent in the 0.2 V < E vs. RHE < 0.6 V region, representing an excellent fill factor, resulted in a photocurrent density of 3.3 ± 0.3 mA/cm² at a potential as low as 0.6 V vs. RHE. Figure 2B shows that the incident photon-to-current conversion efficiency (IPCE) and the absorbed photon-to-current conversion efficiency (APCE) of the nanoporous BiVO₄ at 0.6 V vs. RHE are 60% and 72%, respectively, at 420 nm.

Photocurrent density obtained for sulfite oxidation was used to calculate ϕ_sep using Eq. 1, where J_{PEC} is the measured photocurrent density, and J_{abs} is the photon absorption rate expressed as current density, which is calculated assuming 100% APCE (See Supplementary Materials for calculation details) (*4, 6, 19–21*). J_{abs} of the nanoporous BiVO₄ electrode was calculated to be 4.45 mA/cm². ϕ_sep is the yield of the photogenerated holes that reach the surface and ϕ_ox is the yield of the surface reaching holes that are injected into the solution species (*21*).

$$J_{PEC} = J_{abs} \times \phi_{sep} \times \phi_{ox} \quad (1)$$

For sulfite oxidation with extremely fast oxidation kinetics, surface re-

combination is negligible and ϕ_{ox} is ~ 1. Therefore, ϕ_{sep} is obtained by dividing J_{PEC} by J_{abs} (inset in Fig. 2A). The result shows that the nanoporous $BiVO_4$ electrode achieves ϕ_{sep} = 0.70 ± 0.03 and 0.90 ± 0.03 at 0.6 V and 1.23 V vs. RHE, respectively, which is remarkable as a typical ϕ_{sep} value for a $BiVO_4$ photoanode is below 0.3 at 1.23 V vs. RHE (4, 6). The highest ϕ_{sep} achieved recently by Abdi and co-workers using gradient doping was *ca.* 0.6 at 1.23 V vs. RHE (12). The hole diffusion length of $BiVO_4$ was recently reported to be *ca.* 100 nm using single crystal $BiVO_4$ (22). The mean particle size of $BiVO_4$ composing the nanoporous $BiVO_4$ electrode shown in Fig. 1D is 76 ± 5 nm (fig. S3) and the particle size obtained from the XRD peaks (fig. S5) using the Scherrer equation is 27 ± 2 nm. Therefore, the nanoporosity incorporated into $BiVO_4$ electrodes in this study appears to be ideal for effectively suppressing bulk carrier recombination, resulting in a record high ϕ_{sep}.

Photocurrent from the nanoporous $BiVO_4$ for water oxidation shown in Fig. 3A (black line) is significantly lower than the photocurrent for sulfite oxidation (Fig. 2A), indicating the majority of the surface reaching holes were lost to surface recombination due to the poor catalytic nature of the $BiVO_4$ surface for water oxidation (2). To improve water oxidation kinetics we photodeposited a thin FeOOH or NiOOH layer on the nanoporous $BiVO_4$ surface as an OEC layer to assemble $BiVO_4$/FeOOH and $BiVO_4$/NiOOH electrodes. Their thicknesses were optimized to maximize photocurrent generation (fig. S7). It has been previously demonstrated that FeOOH interfaces well with $BiVO_4$ (13, 15) while NiOOH is known to be a more active OEC than FeOOH (i.e., less overpotential required to achieve the same current density) as a dark electrocatalyst on a conducting substrate (fig. S8) (23–25).

The photocurrents for water oxidation from the resulting $BiVO_4$/FeOOH and $BiVO_4$/NiOOH photoanodes were significantly higher than those from the bare $BiVO_4$ electrode (Fig. 3A, table S2), but their photocurrents were still lower than that generated for sulfite oxidation at the bare $BiVO_4$ electrode. This comparison suggested that neither $BiVO_4$/FeOOH nor $BiVO_4$/NiOOH engages all surface reaching holes in the oxygen evolution reaction, instead losing a portion to surface recombination at the $BiVO_4$/OEC junction. The interface states formed at the $BiVO_4$/OEC junction can serve as recombination centers and cause surface recombination. The fact that $BiVO_4$/FeOOH generated higher photocurrent than $BiVO_4$/NiOOH, although NiOOH shows faster water oxidation kinetics as an electrocatalyst, suggests that the interface recombination at the $BiVO_4$/NiOOH junction is more substantial than that at the $BiVO_4$/FeOOH junction. This can be easily confirmed by comparing photocurrents for sulfite oxidation by $BiVO_4$, $BiVO_4$/FeOOH, and $BiVO_4$/NiOOH (Fig. 3, B and C, table S3). Because the interfacial hole transfer rates for sulfite oxidation on the $BiVO_4$, FeOOH, and NiOOH surfaces should be equally fast, any difference observed in photocurrents for sulfite oxidation by $BiVO_4$, $BiVO_4$/FeOOH, and $BiVO_4$/NiOOH should be mainly due to the recombination at the $BiVO_4$/OEC junction. The comparison shows that photocurrent for $BiVO_4$/FeOOH is very close to that for $BiVO_4$ while the photocurrent for $BiVO_4$/NiOOH is considerably lower, which indicates that the interface recombination at the $BiVO_4$/NiOOH junction is indeed more significant.

In addition to the interface recombination at the $BiVO_4$/OEC junction, slow water oxidation kinetics at the OEC/solution junction can cause additional surface recombination during water oxidation (26, 27). This additional surface recombination can be shown as the difference in photocurrent for sulfite oxidation and water oxidation (Fig. 3, B and C). When the rate of interfacial hole transfer for water oxidation is slower than the rate of holes entering the OEC layer, holes are accumulated in the OEC layer and at the $BiVO_4$/OEC junction, which in turn increases the electron current from the conduction band of $BiVO_4$ to the OEC layer for surface recombination (27). Since FeOOH has slower water oxidation kinetics than NiOOH, the difference in photocurrent for water oxidation and sulfite oxidation is more pronounced for $BiVO_4$/FeOOH

than $BiVO_4$/NiOOH (Fig. 3, B and C). However, when the effects of interface recombination at the $BiVO_4$/OEC junction and water oxidation kinetics are combined, $BiVO_4$/NiOOH loses more surface reaching holes to surface recombination and generates lower photocurrent than $BiVO_4$/FeOOH for water oxidation (Fig. 3A).

Another interesting feature to note is that regardless of more significant surface recombination, $BiVO_4$/NiOOH shows an earlier photocurrent onset and generates higher photocurrent than $BiVO_4$/FeOOH in the low bias region (E < 0.44 V vs. RHE) for water oxidation (Fig. 3A and table S2). This means $BiVO_4$/NiOOH has a more negative flatband potential (E_{FB}) than $BiVO_4$/FeOOH. The photocurrent onset potential for sulfite oxidation with fast oxidation kinetics should be very close to E_{FB}. The results show that $BiVO_4$ has the most negative onset potential (0.11 ± 0.02 V vs. RHE), followed by $BiVO_4$/NiOOH (0.12 ± 0.02 V vs. RHE), and then $BiVO_4$/FeOOH (0.18 ± 0.02 V vs. RHE) (table S3 and fig. S9A). The E_{FB}s obtained by Mott-Schottky plots of $BiVO_4$, $BiVO_4$/FeOOH, and $BiVO_4$/NiOOH show the same trend; $BiVO_4$ has the most negative E_{FB} (0.10 ± 0.03 V vs. RHE), followed by $BiVO_4$/NiOOH (0.11 ± 0.03 V vs. RHE), and then $BiVO_4$/FeOOH (0.15 ± 0.02 V vs. RHE) (table S4 and fig. S10).

It is unlikely that the shift in E_{FB} is due to the change in charge carrier density of $BiVO_4$ as the addition of an extremely thin OEC layer should not affect the doping level or carrier density within the $BiVO_4$ electrode. This assumption is also supported by the comparable slopes in the Mott−Schottky plots for these three electrodes at each frequency (table S4). Then, the difference in E_{FB} should be caused by the change in the Helmholtz layer potential drop (V_H), which is the only other factor that can affect the E_{FB}, as shown in Eq. 2, where ϕ_{SC} is the work function of the semiconductor vs. vacuum and 4.5 is the scale factor relating the H^+/H_2 redox level to vacuum (28). At the $BiVO_4$/electrolyte junction, the dominant charges that affect the solid side of the Helmholtz double layer come from the adsorption of H^+ and OH^- ions on the $BiVO_4$ surface, which depends on the solution pH and the point of zero zeta potential (pH_{PZZP}) of $BiVO_4$ (Eq. 3) (28, 29).

$$E_{FB} (NHE) = \phi_{SC} + V_H - 4.5 \quad (2)$$
$$V_H = 0.059 (pH_{PZZP} - pH) \quad (3)$$

The pH_{PZZP} of $BiVO_4$ is reported to be between 2.5 and 3.5, and, therefore, V_H should be negative in a pH 7 solution (30, 31). However, when a thin layer of FeOOH or NiOOH is deposited on $BiVO_4$, since the Helmholtz double layer is now formed at the OEC/solution junction, the V_H at the solid/solution interface is no longer determined by the pH_{PZZP} of $BiVO_4$ but by the pH_{PZZP} of the OEC layer. This means that the pH_{PZZP} of OEC is an important factor to consider in optimizing the photoanode/OEC junction as it can affect the E_{FB} of the photoanode.

The pH_{PZZP} of FeOOH is reported to be between 7 and 9 (32, 33). Thus, the resulting more positive V_H at the FeOOH/solution junction will shift the E_{FB} of $BiVO_4$/FeOOH positively, in agreement with the observed shift direction of the E_{FB}. The pH_{PZZP} of NiOOH cannot be straightforwardly determined because chemical composition of NiOOH varies with pH. However, it is known that NiOOH has a negative zeta potential (*ca.* -20 mV) in a pH 7 solution (34), meaning that pH_{PZZP} of NiOOH is lower than 7, and the E_{FB} of $BiVO_4$/NiOOH is expected to be more negative than that of $BiVO_4$/FeOOH, which again agrees with the observed E_{FB} shift.

The pH_{PZZP} of a material depends on its specific surface termination and solution composition. Therefore, the most reliable estimations of the V_Hs of electrodes discussed in this study can be obtained when the zeta potential measurement is performed using the electrodes and the solution that were used in this study. The zeta potentials measured for our nanoporous $BiVO_4$, $BiVO_4$/FeOOH and $BiVO_4$/NiOOH in a 0.5 M phosphate buffer (pH 7) were -36 ± 3 mV, -8 ± 3 mV, and -36 ± 4 mV, respectively. These results indicate that the V_Hs at the $BiVO_4$/solution and the NiOOH/solution junctions should indeed be more negative than

that at the FeOOH/solution junction.

Based on our new understanding of the BiVO$_4$/OEC and the OEC/electrolyte interfaces, we deposited consecutive layers of FeOOH and NiOOH, simultaneously optimizing the BiVO$_4$/OEC and the OEC/electrolyte junctions. The FeOOH at the BiVO$_4$/OEC junction will reduce the interface recombination while the NiOOH at the OEC/electrolyte junction will decrease V$_H$ to achieve a more negative E$_{FB}$ for BiVO$_4$ while realizing faster water oxidation kinetics than if FeOOH was used as the outermost layer.

The photocurrent onset for sulfite oxidation (fig. S9A, table S3) as well as the Mott-Schottky plot (fig. S10, table S4) of the resulting Bi-VO$_4$/FeOOH/NiOOH photoanode shows that its E$_{FB}$ is comparable to that of BiVO$_4$/NiOOH, indicating that the E$_{FB}$ of the BiVO$_4$ photoanode is indeed affected by the pH$_{PZZP}$ of the outermost OEC layer. In addition, BiVO$_4$/FeOOH/NiOOH and BiVO$_4$/FeOOH show comparable J-V curves for sulfite oxidation, confirming that the BiVO$_4$/FeOOH junction effectively reduces the interface recombination at the BiVO$_4$/OEC junction (Fig. 3, B and D). As a result, BiVO$_4$/FeOOH/NiOOH shows impressive overall performance for water oxidation, reaching a photocurrent density of 2.8 $\pm$ 0.2 mA/cm^2 at 0.6 V vs. RHE (Fig. 3A, table S2), which is markedly better than those of BiVO$_4$/FeOOH and BiVO$_4$/NiOOH and is almost comparable to the performance of bare BiVO$_4$ for sulfite oxidation.

When NiOOH was first deposited on the BiVO$_4$ surface and FeOOH was added as the outermost layer to form BiVO$_4$/NiOOH/FeOOH (i.e., reversed OEC junction), the resulting E$_{FB}$s determined by sulfite photocurrent onset (fig. S9A, table S3) and Mott-Schottky plot (fig. S10, table S4) are comparable to those of BiVO$_4$/FeOOH, again confirming that the E$_{FB}$ of the BiVO$_4$ photoanode is affected by the pH$_{PZZP}$ of the outermost OEC. Also, the J-V curve for sulfite oxidation by Bi-VO$_4$/NiOOH/FeOOH was comparable to that by BiVO$_4$/NiOOH, confirming that BiVO$_4$/NiOOH junction is not favorable for interface recombination (Fig. 3, C and E). As a result, BiVO$_4$/NiOOH/FeOOH shows the lowest photocurrent for water oxidation. These results prove that the photocurrent enhancement achieved by the Bi-VO$_4$/FeOOH/NiOOH photoanode for photoelectrolysis of water is truly due to the simultaneous optimization of the BiVO$_4$/OEC and OEC/electrolyte junctions using an optimum dual OEC structure.

The applied bias photon-to-current efficiency (ABPE) of the Bi-VO$_4$/FeOOH/NiOOH electrode calculated using its J-V curve assuming 100% Faradaic efficiency is plotted in Fig. 4A (35). The maximum ABPE of 1.75% achieved by the system is impressive, as it is obtained by using unmodified BiVO$_4$ as a single photon absorber. Moreover, this efficiency is achieved at a potential as low as 0.6 V vs. RHE, which is a highly favorable feature for assembling a tandem cell or a photoelectro-chemical diode (12, 36, 37). The ABPE obtained using a two-electrode system (working electrode and a Pt counter electrode), which achieves the maximum ABPE of 1.72%, is also shown in fig. S11 (35). The long-term stability of BiVO$_4$/FeOOH/NiOOH was tested by obtaining a J-t curve. Figure 4B shows that a photocurrent density of 2.73 mA/cm^2, obtained by applying 0.6 V between the working and counter electrodes, was maintained for 48 hours without showing any sign of decay, proving its long-term stability. The O$_2$ measurement using a fluorescence O$_2$ sensor confirmed that the photocurrent generated at 0.6 V vs. counter electrode was mainly associated with O$_2$ production (> 90% photocur-rent-to-O$_2$ conversion efficiency) (Fig. 4C). The same results were obtained when the measurement was performed at 0.6 V vs. RHE. H$_2$ production at the Pt counter electrode was also detected using gas chro-matography (GC) (Fig. 4C). The molar ratio of the produced H$_2$:O$_2$ was 1.85:1. The slight deviation from the stoichiometric ratio of 2:1 is due to our imperfect manual sampling method of H$_2$ for GC analysis.

Because this outstanding performance was achieved by using simple, unmodified BiVO$_4$ (i.e., no extrinsic doping, no composition tuning) as

the only photon absorber, further improvement of the cell efficiency is expected when various strategies of tuning compositions or forming heterojunctions and tandem cells are employed to enhance photon ab-sorption and electron-hole separation.

References and Notes
1. A. Kudo, K. Omori, H. Kato, A novel aqueous process for preparation of crystal form-controlled and highly crystalline BiVO$_4$ powder from layered vanadates at room temperature and its photocatalytic and photophysical properties. *J. Am. Chem. Soc.* **121**, 11459–11467 (1999). doi:10.1021/ja992541y
2. Y. Park, K. J. McDonald, K.-S. Choi, Progress in bismuth vanadate photoanodes for use in solar water oxidation. *Chem. Soc. Rev.* **42**, 2321–2337 (2013). doi:10.1039/c2cs35260e Medline
3. Y. Liang, T. Tsubota, L. P. A. Mooij, R. van de Krol, Highly improved quantum efficiencies for thin film BiVO$_4$ photoanodes. *J. Phys. Chem. C* **115**, 17594–17598 (2011). doi:10.1021/jp203004v
4. F. F. Abdi, R. van de Krol, Nature and light dependence of bulk recombination in Co-Pi-catalyzed BiVO$_4$ photoanodes. *J. Phys. Chem. C* **116**, 9398–9404 (2012). doi:10.1021/jp3007552
5. F. F. Abdi, T. J. Savenije, M. M. May, B. Dam, R. van de Krol, The origin of slow carrier transport in BiVO$_4$ thin film photoanodes: A time-resolved microwave conductivity Study. *J. Phys. Chem. Lett* **4**, 2752–2757 (2013). doi:10.1021/jz4013257
6. D. K. Zhong, S. Choi, D. R. Gamelin, Near-complete suppression of surface recombination in solar photoelectrolysis by "Co-Pi" catalyst-modified W:BiVO$_4$. *J. Am. Chem. Soc.* **133**, 18370–18377 (2011). doi:10.1021/ja207348x Medline
7. H. S. Park, K. E. Kweon, H. Ye, E. Paek, G. S. Hwang, A. J. Bard, Factors in the metal doping of BiVO$_4$ for improved photoelectrocatalytic activity as studied by scanning electrochemical microscopy and first-principles density-functional calculation. *J. Phys. Chem. C* **115**, 17870–17879 (2011). doi:10.1021/jp204492r
8. W. J. Jo, J. W. Jang, K. J. Kong, H. J. Kang, J. Y. Kim, H. Jun, K. P. Parmar, J. S. Lee, Phosphate doping into monoclinic BiVO$_4$ for enhanced photoelectrochemical water oxidation activity. *Angew. Chem. Int. Ed. Engl.* **51**, 3147–3151 (2012). doi:10.1002/anie.201108276 Medline
9. S. P. Berglund, A. J. E. Rettie, S. Hoang, C. B. Mullins, Incorporation of Mo and W into nanostructured BiVO(4) films for efficient photoelectrochemical water oxidation. *Phys. Chem. Chem. Phys.* **14**, 7065–7075 (2012). doi:10.1039/c2cp40807d Medline
10. K. Zhang, X. J. Shi, J. K. Kim, J. H. Park, Photoelectrochemical cells with tungsten trioxide/Mo-doped BiVO$_4$ bilayers. *Phys. Chem. Chem. Phys.* **14**, 11119–11124 (2012). doi:10.1039/c2cp40991g Medline
11. Y. Park, D. Kang, K.-S. Choi, Marked enhancement in electron-hole separation achieved in the low bias region using electrochemically prepared Mo-doped BiVO$_4$ photoanodes. *Phys. Chem. Chem. Phys.* **16**, 1238–1246 (2014). doi:10.1039/c3cp53649a Medline
12. F. F. Abdi, L. Han, A. H. Smets, M. Zeman, B. Dam, R. van de Krol, Efficient solar water splitting by enhanced charge separation in a bismuth vanadate-silicon tandem photoelectrode. *Nat. Commun* **4**, 2195 (2013). doi:10.1038/ncomms3195 Medline
13. K. J. McDonald, K.-S. Choi, A new electrochemical synthesis route for a BiOI electrode and its conversion to a highly efficient porous BiVO$_4$ photoanode for solar water oxidation. *Energy Environ. Sci* **5**, 8553–8557 (2012). doi:10.1039/c2ee22608a
14. T. Allen, *Particle Size Measurement* (Chapman and Hall, London, 1997).
15. J. A. Seabold, K.-S. Choi, Efficient and stable photo-oxidation of water by a bismuth vanadate photoanode coupled with an iron oxyhydroxide oxygen evolution catalyst. *J. Am. Chem. Soc.* **134**, 2186–2192 (2012). doi:10.1021/ja209001d Medline
16. R. Sarala, M. A. Islam, S. B. Rabin, D. M. Stanbury, Aromatic sulfonation by sulfite and the reduction potential of the sulfite radical: oxidation of sulfite by the tetraammine(phenanthroline)ruthenium(II) cation. *Inorg. Chem.* **29**, 1133–1142 (1990). doi:10.1021/ic00331a006
17. D. M. Stanbury, Reduction potentials involving inorganic free radicals in aqueous solution. *Adv. Inorg. Chem.* **33**, 69–138 (1989).
18. J.-F. Reber, K. Meier, Photochemical production of hydrogen with zinc sulfide suspensions. *J. Phys. Chem.* **88**, 5903–5913 (1984).

doi:10.1021/j150668a032

19. H. Dotan, K. Sivula, M. Grätzel, A. Rothschild, S. C. Warren, Probing the photoelectrochemical properties of hematite (α-Fe$_2$O$_3$) electrodes using hydrogen peroxide as a hole scavenger. *Energy Environ. Sci* **4**, 958–964 (2011). doi:10.1039/c0ee00570c

20. J. M. Foley, M. J. Price, J. I. Feldblyum, S. Maldonado, Analysis of the operation of thin nanowire photoelectrodes for solar energy conversion. *Energy Environ. Sci* **5**, 5203–5220 (2012). doi:10.1039/c1ee02518j

21. M. Zhou, J. Bao, W. Bi, Y. Zeng, R. Zhu, M. Tao, Y. Xie, Efficient water splitting via a heteroepitaxial BiVO($_4$) photoelectrode decorated with Co-Pi catalysts. *ChemSusChem* **5**, 1420–1425 (2012). doi:10.1002/cssc.201200287 Medline

22. A. J. E. Rettie, H. C. Lee, L. G. Marshall, J. F. Lin, C. Capan, J. Lindemuth, J. S. McCloy, J. Zhou, A. J. Bard, C. B. Mullins, Combined charge carrier transport and photoelectrochemical characterization of BiVO$_4$ single crystals: intrinsic behavior of a complex metal oxide. *J. Am. Chem. Soc.* **135**, 11389–11396 (2013). doi:10.1021/ja405550k Medline

23. L. Trotochaud, J. K. Ranney, K. N. Williams, S. W. Boettcher, Solution-cast metal oxide thin film electrocatalysts for oxygen evolution. *J. Am. Chem. Soc.* **134**, 17253–17261 (2012). doi:10.1021/ja307507a Medline

24. R. D. L. Smith, M. S. Prévot, R. D. Fagan, Z. Zhang, P. A. Sedach, M. K. Siu, S. Trudel, C. P. Berlinguette, Photochemical route for accessing amorphous metal oxide materials for water oxidation catalysis. *Science* **340**, 60–63 (2013). doi:10.1126/science.1233638 Medline

25. M. W. Louie, A. T. Bell, An investigation of thin-film Ni-Fe oxide catalysts for the electrochemical evolution of oxygen. *J. Am. Chem. Soc.* **135**, 12329–12337 (2013). doi:10.1021/ja405351s Medline

26. C. Y. Cummings, F. Marken, L. M. Peter, A. A. Tahir, K. G. Wijayantha, Kinetics and mechanism of light-driven oxygen evolution at thin film α-Fe$_2$O$_3$ electrodes. *Chem. Commun. (Camb.)* **48**, 2027–2029 (2012). doi:10.1039/c2cc16382a Medline

27. L. M. Peter, K. G. Wijayantha, A. A. Tahir, Kinetics of light-driven oxygen evolution at α-Fe$_2$O$_3$ electrodes. *Faraday Discuss.* **155**, 309–322, discussion 349–356 (2012). doi:10.1039/c1fd00079a Medline

28. J. Nozik, Photoelectrochemisty: applications to solar energy conversion. *Annu. Rev. Phys. Chem.* **29**, 189–222 (1978). doi:10.1146/annurev.pc.29.100178.001201

29. S. R. Morrison, Electrochemistry at Semiconductor and Oxidized Metal Electrodes (Plenum Press: New York, 1980, p49-78).

30. N. C. Castillo, A. Heel, T. Graule, C. Pulgarin, Flame-assisted synthesis of nanoscale, amorphous and crystalline, spherical BiVO$_4$ with visible-light photocatalytic activity. *Appl. Catal. B* **95**, 335–347 (2010). doi:10.1016/j.apcatb.2010.01.012

31. S. Obregón, G. Colón, On the different photocatalytic performance of BiVO$_4$ catalysts for Methylene Blue and Rhodamine B degradations. *J. Mol. Catal. Chem.* **376**, 40–47 (2013). doi:10.1016/j.molcata.2013.04.012

32. R. M. Cornell, U. Schwertmann, The Iron Oxides: Structure, Properties, Reactions, Occurrences and Uses (Wiley VCH, New York, 2003).

33. D. M. Sherman, Electronic structures of iron(III) and manganese(IV) (hydr)oxide minerals: Thermodynamics of photochemical reductive dissolution in aquatic environments. *Geochim. Cosmochim. Acta* **69**, 3249–3255 (2005). doi:10.1016/j.gca.2005.01.023

34. N. Hernández, R. Moreno, A. J. Sánchez-Herencia, J. L. Fierro, Surface behavior of nickel powders in aqueous suspensions. *J. Phys. Chem. B* **109**, 4470–4474 (2005). doi:10.1021/jp0448954 Medline

35. Z. Chen, T. F. Jaramillo, T. G. Deutsch, A. Kleiman-Shwarsctein, A. J. Forman, N. Gaillard, R. Garland, K. Takanabe, C. Heske, M. Sunkara, E. W. McFarland, K. Domen, E. L. Miller, J. A. Turner, H. N. Dinh, Accelerating materials development for photoelectrochemical hydrogen production: Standards for methods, definitions, and reporting protocols. *J. Mater. Res.* **25**, 3–16 (2010). doi:10.1557/JMR.2010.0020

36. M. G. Walter, E. L. Warren, J. R. McKone, S. W. Boettcher, Q. Mi, E. A. Santori, N. S. Lewis, Solar water splitting cells. *Chem. Rev.* **110**, 6446–6473 (2010). doi:10.1021/cr1002326 Medline

37. L. Tong, A. Iwase, A. Nattestad, U. Bach, M. Weidelener, G. Götz, A. Mishra, P. Bäuerle, R. Amal, G. G. Wallace, A. J. Mozer, Sustained solar hydrogen generation using a dye-sensitised NiO photocathode/BiVO$_4$ tandem photo-electrochemical device. *Energy Environ. Sci* **5**, 9472–9475 (2012). doi:10.1039/c2ee22866a

38. L. Zhang, Y. Zhong, Z. He, J. Wang, J. Xu, J. Cai, N. Zhang, H. Zhou, H. Fan, H. Shao, J. Zhang, C.- Cao, Surfactant-assisted photochemical deposition of three-dimensional nanoporous nickel oxyhydroxide films and their energy storage and conversion properties. *J. Mater. Chem. A* **1**, 4277–4285 (2013). doi:10.1039/c3ta00968h

39. G. W. D. Briggs, M. Fleischmann, Anodic deposition of NiOOH from nickel acetate solutions at constant potential. *Trans. Faraday Soc.* **62**, 3217–3228 (1966). doi:10.1039/tf9666203217

40. ASTM Standard G173 - 03, 2008, "Standard Tables for Reference Solar Spectral Irradiances: Direct Normal and Hemispherical on 37° Tilted Surface," ASTM International, West Conshohocken, PA, 2003, DOI: 10.1520/G0173-03R08, www.astm.org.

41. K. Sayama, A. Nomura, T. Arai, T. Sugita, R. Abe, M. Yanagida, T. Oi, Y. Iwasaki, Y. Abe, H. Sugihara, Photoelectrochemical decomposition of water into H$_2$ and O$_2$ on porous BiVO$_4$ thin-film electrodes under visible light and significant effect of Ag ion treatment. *J. Phys. Chem. B* **110**, 11352–11360 (2006). doi:10.1021/jp057539+ Medline

Supplementary Materials
www.sciencemag.org/content/science.1246913/DC1
Materials and Methods
Figs. S1 to S11
Tables S1 to S4
References (*38–41*)
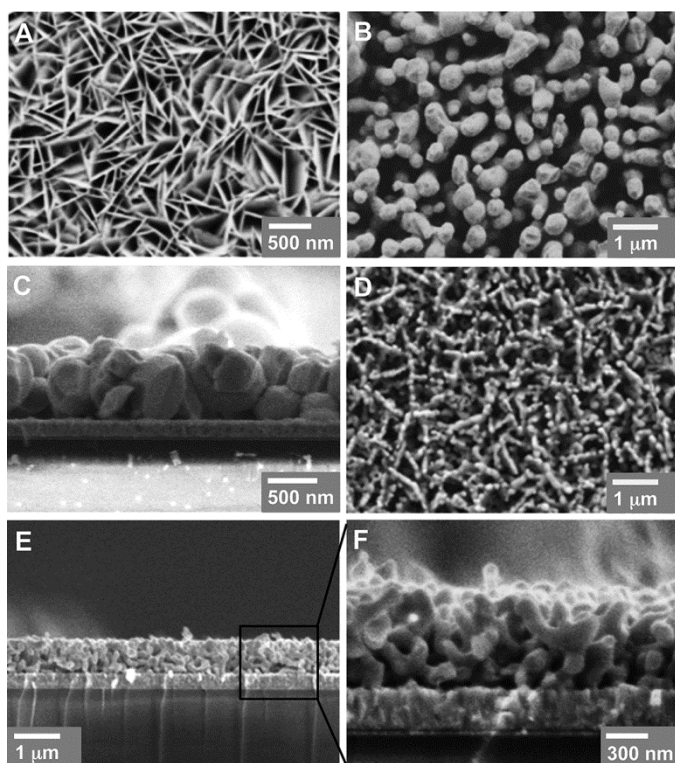
Fig. 1. Morphologies of nanoporous BiVO₄ electrodes. (**A**) SEM image of BiOI, (**B** and **C**) Top-view and side-view SEM images of BiVO₄ electrode prepared using NH₄OH/V₂O₅, (**D** to **F**) Top-view and side-view SEM images of nanoporous BiVO₄ prepared using DMSO/VO(acac)₂.
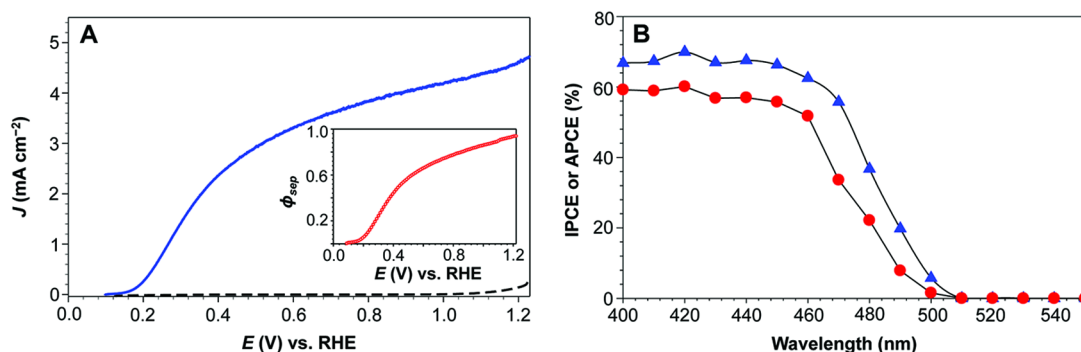
Fig. 2. Photoelectrochemical properties of nanoporous BiVO₄ electrode for sulfite oxidation. (**A**) J-V curve of nanoporous BiVO₄ electrode measured in a 0.5 M phosphate buffer (pH 7) containing 1 M Na₂SO₃ as hole scavenger under AM 1.5 G, 100 mW/cm² illumination (scan rate, 10 mV/s). Dark current is shown as dashed line. The inset shows ϕ_{sep} calculated from the J-V curve after dark current is subtracted. (**B**) IPCE (red circles) and APCE (blue triangles) measured in the same solution at 0.6 V vs. RHE.

Fig. 3. Effect of OECs on photocurrents for water oxidation and sulfite oxidation. (**A**) J-V curves of $BiVO_4$ (black solid), $BiVO_4/FeOOH$ (blue), $BiVO_4/NiOOH$ (green), $BiVO_4/FeOOH/NiOOH$ (red), and $BiVO_4/NiOOH/FeOOH$ (pink) for water oxidation measured in a 0.5 M phosphate buffer (pH 7) under AM 1.5G illumination. J-V curves of (**B**) $BiVO_4/FeOOH$, (**C**) $BiVO_4/NiOOH$, (**D**) $BiVO_4/FeOOH/NiOOH$, and (**E**) $BiVO_4/NiOOH/FeOOH$ comparing photocurrent for sulfite oxidation (dashed) and water oxidation (solid) measured with and without the presence of 1.0 M Na_2SO_3 as hole scavenger. Photocurrent for sulfite oxidation by $BiVO_4$ is shown as the black dashed line for comparison. The mean values and standard deviations of photocurrent onset potentials and photocurrent densities are summarized in tables S2-3.
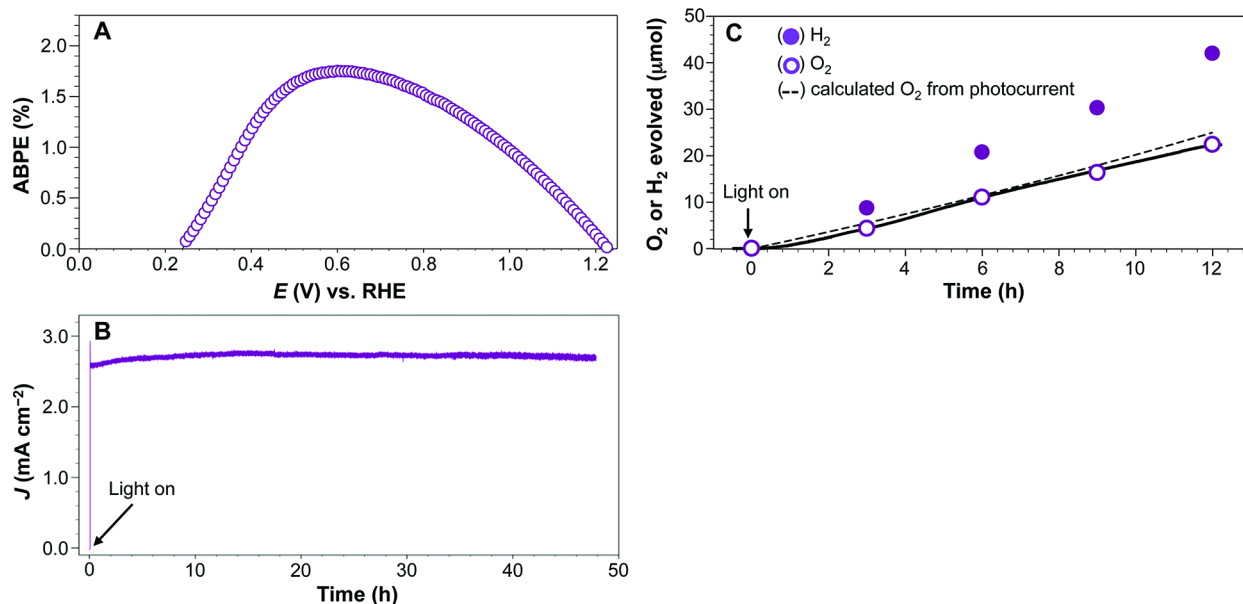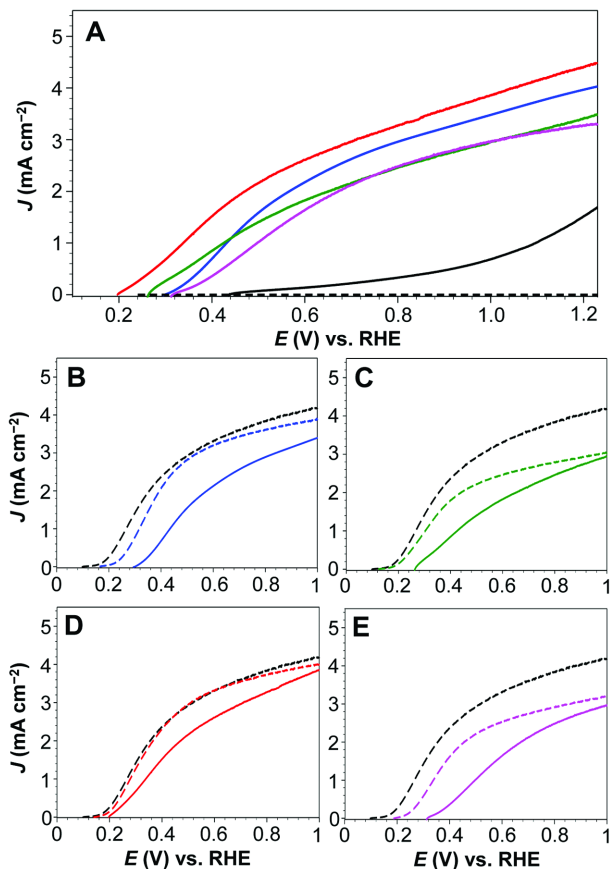
Fig. 4. Photoelectrolysis of water by BiVO₄/FeOOH/NiOOH photoanode. (**A**) ABPE obtained using a three-electrode system. (**B**) J-t curve measured at 0.6 V vs. counter electrode in a phosphate buffer (pH 7) under AM 1.5G illumination. (**C**) Detection of H_2 and O_2 at 0.6 V vs. counter electrode.